Catalysis Science & Technology

ROYAL SOCIETY OF CHEMISTRY

PAPER

View Article Online
View Journal | View Issue

Cite this: *Catal. Sci. Technol.*, 2026, **16**, 1677

Cobalt-doped $ZnIn_2S_4$ for highly efficient photocatalytic oxidation of 5-hydroxymethylfurfural to 2,5-diformylfuran

Xiaohan Xing,[a] Xu Tang,*[a] Zhi Zhu,*[ab] Binrong Li,*[c] Yixuan Liu,[b] Wenhua Xue,[b] Pengwei Huo [a] and Jun Zhao *[b]

Received 7th November 2025,
Accepted 14th January 2026

DOI: 10.1039/d5cy01322d

rsc.li/catalysis

The photocatalytic transformation of 5-hydroxymethylfurfural (HMF) into high-value chemicals has been widely studied; however, selectively converting HMF to the valuable chemical 2,5-diformylfuran (DFF) remains challenging. In this work, we explored the doping of transition metal Co into $ZnIn_2S_4$ and systematically investigated the photocatalytic conversion of HMF to DFF. Doping transition metal Co into $ZnIn_2S_4$ significantly enhances its catalytic activity for converting HMF to DFF, achieving a yield of 88%, and the selectivity approaches 90%, which is significantly higher than that of pure $ZnIn_2S_4$, thus improving HMF utilization. Electron spin resonance (ESR) experiments show that doping Co promotes the formation of singlet oxygen ($^1O_2$) and superoxide radicals ($\cdot O_2^-$). Density functional theory (DFT) calculations suggest that introducing Co reduced the surface binding energy between DFF and the catalyst, and accelerated the desorption of DFF from the Co/ZIS surface, improving active site utilization and enhancing HMF-to-DFF conversion activity. Also, *in situ* FTIR and DFT studied the surface O_2 adsorption behavior. This work presents an effective strategy for constructing a novel, low-cost photocatalytic system, providing new insights into HMF transformation into high-value chemicals.

1. Introduction

The excessive consumption of fossil fuels has led to an escalating energy crisis and global warming. As a result, reducing dependence on fossil fuels and exploring renewable carbon resources have become an urgent priority.[1–3] Biomass materials, abundant and renewable, are widely available and rich in raw materials, making them promising candidates for addressing the energy crisis.[4] Among the various biomass-derived furan compounds, 5-hydroxymethylfurfural (HMF) is considered an important platform molecule in the biorefining process.[5,6] Starting with HMF as the raw material, a series of products can be obtained through transformation, including 2,5-furandicarboxylic acid (FDCA), 2,5-diformylfuran (DFF), 5-hydroxymethyl-2-furancarboxylic acid (HMFCA), and 5-formyl-2-furancarboxylic acid (FFCA).[7] Among them, DFF is a high-value chemical compound containing two active groups: an aldehyde group and a furan ring. DFF is widely used in the synthesis of fluorescent materials, pharmaceutical compounds, and polymers containing furan rings.[8–10]

In recent years, the rapid development of photocatalytic technology has led to its widespread application in pollutant degradation, hydrogen production, and CO_2 reduction.[11–17] The photocatalytic valorization of HMF has attracted significant attention from researchers. Generally, HMF valorization *via* photocatalytic methods can be categorized into two pathways: aerobic and anaerobic. In the anaerobic photocatalytic reaction of HMF, hydrogen gas is an inevitable by-product.[18–21] $ZnIn_2S_4$ (ZIS), a bimetallic sulfide, is an emerging semiconductor photocatalyst with a low bandgap (2.06–2.85 eV), allowing rapid response to visible light, short carrier migration distances, low toxicity, and good chemical stability, making it a promising candidate for next-generation semiconductor photocatalysts.[22–24] To date, various strategies, including surface modification, heteroatom doping, and heterostructure construction, have been employed to improve ZIS reactivity.[25–29] Zhu *et al.*[30] synthesized oxygen-doped ZIS nanosheets using an *in situ* topotactic transformation method, converting HMF to DFF with concomitant stoichiometric H_2 production. However, this process is hindered by low HMF

[a] *Institute for Advanced Materials, School of Chemistry and Chemical Engineering, Jiangsu University, Zhenjiang 212013, China. E-mail: tangxu@ujs.edu.cn, zhuzhi@hkbu.edu.hk*
[b] *Applied Research Centre for Pearl River Delta Environment, Department of Biology, Hong Kong Baptist University, Hong Kong, SAR, China. E-mail: zhaojun@hkbu.edu.hk*
[c] *National and Local Joint Engineering Laboratory of Municipal Sewage Resource Utilization Technology, School of Environmental Science and Engineering, Suzhou University of Science and Technology, Suzhou, 215009, China. E-mail: libr@usts.edu.cn*

conversion rates. To enhance HMF conversion rates, it is essential to introduce additional reactive oxygen species (ROS) to facilitate the transformation.[31–33] Zhang *et al.*[31] synthesized an $MAPbBr_3$ and used photocatalytic HMF to selectively oxidize to DFF using 450 nm blue LED light. The conversion rate of HMF reached 100%, the selectivity to DFF reached 90%, and the yield reached 90%. Guo *et al.*[33] engineered a novel photocatalytic system by immobilizing a specific supramolecular compound, SA-PDI, onto $ZnIn_2S_4$. SA-PDI, functioning as an oxygen reduction cocatalyst, adeptly captures oxygen and channels the photogenerated electrons from $ZnIn_2S_4$, thereby expediting the formation of $\cdot O_2^-$. This system efficiently oxidizes HMF molecules within a span of 30 minutes, achieving an impressive HMF conversion rate of 97.7%, accompanied by a DFF selectivity of 89.8%.

Significant advancements have been made in photocatalysis with HMF molecules under aerobic oxidation conditions. However, several key issues remain: the lack of suitable active sites limits the activation of molecular oxygen, resulting in suboptimal yields and selectivity to the target products in most cases. Metal-ion doping enables multiplicative gains by concurrently tailoring energy-level alignment, accelerating charge transfer, narrowing the bandgap, extending the photoresponse window, suppressing carrier recombination, and elevating electron density.[54,55] Cobalt-based photocatalysts have emerged as mainstream candidates in photocatalysis by virtue of their exceptional stability, low cost, and broad applicability.[56] In this regard, transition metal Co is undoubtedly a metal that can effectively modify ZIS for conversion of HMF to DFF. This alteration could activate molecular oxygen, facilitating the further conversion of HMF to the higher-value product DFF through ROS, thereby achieving high selectivity. Key factors influencing DFF selectivity, particularly ROS and surface binding energy, require thorough investigation through advanced *in situ* characterization techniques and theoretical simulations. Such studies are crucial for elucidating the catalytic mechanisms governing the Co/ZIS-mediated photocatalytic oxidation of HMF.

In this study, hierarchical Co-doped ZIS nanostructures were fabricated through a facile one-pot hydrothermal strategy. The optimized photocatalyst demonstrated exceptional catalytic performance in aerobic oxidation systems, reaching 98% HMF conversion with an 88% DFF yield under visible-light irradiation in oxygenated environments. To elucidate the mechanistic role of cobalt dopants in governing reaction selectivity, we employed a multimodal characterization approach: carrier dynamics were analyzed through photoelectrochemical measurements and time-resolved photoluminescence decay, while surface interactions were modeled *via* DFT simulations. The Co dopant serves dual functions: (1) improving charge separation efficiency through enhanced carrier mobility and (2) modulating surface chemistry to promote DFF desorption *via* optimized adsorption energies. This synergistic effect enables simultaneous high substrate conversion and product selectivity (~90% DFF yield), attributed to accelerated active site regeneration during photocatalytic reactions.

2. Experimental

2.1 Synthesis of $ZnIn_2S_4$ and Co–ZIS-*x* photocatalysts

Cobalt-modified $ZnIn_2S_4$ (Co/ZIS) nanoflowers were prepared using a hydrothermal approach.[34] In a typical synthesis, cobalt nitrate hexahydrate was first dissolved in 30 mL of a binary solvent system consisting of dimethylformamide (DMF) and ethylene glycol (EG) in a 1 : 1 volume ratio. Subsequently, stoichiometric amounts of $ZnCl_2$ (1 mmol), $InCl_3{\cdot}4H_2O$ (2 mmol), and an excess of thioacetamide (2× molar ratio relative to sulfur content) were introduced into the solution. The cobalt loading was systematically varied at nominal mass fractions of 1%, 2%, 3%, and 4%. The mixture was magnetically stirred for 4 h to ensure homogeneity before being sealed in a 50 mL Teflon-lined autoclave and maintained at 180 °C for 24 h. The resulting solid products were collected, thoroughly washed with deionized water and ethanol, and then dried at 60 °C to yield the final Co-doped samples (designated as Co/ZIS-1 to Co/ZIS-4). For comparison, undoped $ZnIn_2S_4$ (ZIS) nanoflowers were synthesized following an identical protocol, omitting the addition of the cobalt precursor.

2.2 Characterization

The structural properties of the synthesized catalysts were systematically investigated through multiple analytical techniques. Morphological evaluation was conducted using field emission scanning electron microscopy (JEOL JSM-7900F) with energy-dispersive X-ray spectroscopy for elemental mapping. Complementary nanoscale imaging was performed through transmission electron microscopy (TEM, JEOL JEM100-CXII). Crystalline phase identification was achieved by X-ray diffraction analysis (Rigaku Smart Lab3) employing Cu Kα radiation (λ = 1.5406 Å), with angular scanning from 10° to 80° (2θ) at a ramp rate of 6° min^{-1}. X-ray photoelectron spectroscopy (XPS, Shimadzu AXIS-ULTRA) with monochromatic Al Kα excitation (1486.6 eV) was used to study the surface chemical states. Optical properties were assessed through UV-vis diffuse reflectance spectroscopy (Persee TU-1901) across 200–1000 nm wavelengths. Textural parameters including specific surface area were determined by nitrogen physisorption measurements at 77 K (Micromeritics ASAP2020HD88), employing the Brunauer–Emmett–Teller (BET) theory for quantitative analysis. Photophysical characteristics were examined using fluorescence spectroscopy (Edinburgh FLS920) with 400 nm excitation from a 450 W Xe arc lamp, recording emission spectra between 450 and 700 nm. Spin trapping experiments utilized electron paramagnetic resonance spectroscopy (JEOL JES-FA300) operating at 9.85 GHz microwave frequency under ambient conditions (300 K).

2.3 Electrochemical measurements

Photoelectrochemical experiments were conducted using a CHI 660E electrochemical workstation, following a traditional three-electrode configuration. In this setup, a 0.5 M Na_2SO_4 aqueous solution served as the electrolyte, with an Ag/AgCl

electrode (saturated KCl) as the reference and a platinum plate as the counter electrode. To prepare the working electrodes for photocurrent and electrochemical impedance spectroscopy (EIS), 0.05 g of photocatalyst and 0.01 g of PVP were mixed with 3 mL of ethanol, and then thoroughly dispersed. After adding 0.03 mL of oleic acid, the mixture was sonicated for 2 hours and spin-coated onto 1.0 cm^2 indium–tin-oxide (ITO) substrates. The working, reference, and counter electrodes were connected appropriately (for photocurrent measurements, a light source and a dotting timer set to 30 seconds were also connected). The electrochemical workstation was activated, the appropriate test mode was selected, and parameters were adjusted to initiate the test.

2.4 DFT computation details

The DFT calculations for structural optimization were carried out using the Vienna *ab initio* simulation package (VASP). The exchange–correlation energy was modeled using the PBE exchange–correlation function within the generalized gradient approximation (GGA). A plane-wave kinetic-energy cutoff of 400 eV was applied, along with a maximum force tolerance of 0.05 eV $Å^{-1}$, to ensure thorough convergence. To prevent interactions between periodic slab images, a vacuum thickness of 20 Å was maintained in the *z*-direction.

2.5 Photocatalytic HMF oxidation

The oxidation of 5-hydroxymethylfurfural (HMF) was conducted in a batch-type photochemical reactor illuminated by a 450 nm LED light source. In a standard procedure, 20 mg of the photocatalyst was suspended in 5 mL of acetonitrile (ACN) containing 10 mM HMF within a 20 mL reaction vessel. Prior to illumination, the mixture underwent 5 minutes of sonication to ensure uniform dispersion, followed by oxygen saturation through continuous bubbling for 10 minutes to establish an oxygen-enriched reaction environment. Samples were taken after a certain reaction time. The cyclic testing was also performed with a standard concentration of 10 mM.

Quantification of 5-hydroxymethylfurfural (HMF), 2,5-diformylfuran (DFF), 5-formyl-2-furancarboxylic acid (FFCA) and 2,5-furandicarboxylic acid (FDCA) was performed using an Agilent 1260 Infinity II chromatographic system equipped with a UV-vis detector. HMF conversion efficiency and DFF selectivity were mathematically derived using the following equations:

$$\text{Conversion}\ (\%) = \frac{C_{\text{HMF},0} - C_{\text{HMF}}}{C_{\text{HMF},0}} \times 100\% \quad (1)$$

$$\text{Yield}\ (\%) = \frac{C_{\text{DFF}}}{C_{\text{HMF},0}} \times 100\% \quad (2)$$

$$\text{Selectivity}\ (\%) = \frac{C_{\text{DFF}}}{C_{\text{HMF},0} - C_{\text{HMF}}} \times 100\% \quad (3)$$

More experimental details can be found in the SI.

3. Results and discussion

3.1 Characterization of Co/ZIS-*x* catalysts

Fig. 1a shows the preparation method of Co/ZIS-*x* catalysts. The morphological characterization of the synthesized material was performed using scanning electron microscopy (SEM) and transmission electron microscopy (TEM). SEM observations (SI Fig. S3) showed that the pristine ZIS formed nanoflowers assembled from nanosheets, with the individual nanoleaves displaying a fluffy architecture on the surface. The Co^{2+}-doped ZIS retained its nanoflower-like structure, as shown in Fig. 1b and c, suggesting that Co^{2+} incorporation does not disrupt the ZIS morphology. High-resolution transmission electron microscopy (HRTEM) revealed interplanar spacings of 0.19 nm, 0.305 nm, and 0.321 nm, corresponding to the (110), (008), and (102) planes of hexagonal ZIS, as shown in Fig. 1d–g, respectively.[35] The elemental mapping results in SI Fig. S4 and 1h–l show that Co, In, Zn, and S elements are uniformly distributed across the material, closely matching the apparent molar ratios from the synthesis. This confirms the successful synthesis of Co/ZIS-2 nanoflowers.

XPS was utilized to precisely evaluate the state of the Co element present in Co-ZIS, with all binding energies calibrated to the C 1s peak at 284.8 eV. In the survey spectra of Fig. 2a, both ZIS and Co/ZIS-2 show strong characteristic peaks for S, In, and Zn, consistent with the composition of ZIS. High-resolution spectral scans were performed for each element to gain a more precise understanding of their chemical environment, as shown in Fig. 2b–d. The two peaks of ZIS, located at 161 eV and 162.1 eV, correspond to the S 2p orbitals of $2p_{3/2}$ and $2p_{1/2}$, respectively.[36] The two peaks at 444.4 eV and 451.9 eV correspond to the In $3d_{5/2}$ and In $3d_{3/2}$ orbitals, respectively, while the peaks at 1021.1 eV and 1044.2 eV correspond to the Zn $2p_{3/2}$ and Zn $2p_{1/2}$ orbitals, indicating the presence of Zn^{2+}.[37,38] Compared to ZIS, the XPS spectra of S 2p, Zn 2p, and In 3d for Co-doped ZIS show an increase in binding energy, indicating changes in the electronic structure and chemical interactions in Co/ZIS-2, as seen in Fig. 2b–d. The increase in binding energy of the S 2p orbital may be due to the weaker electron-donating ability of Co compared to Zn. Upon doping, the electron density around the sulfur atoms decreases, resulting in the upward shift of the S 2p peaks.[35] The increase in Zn 2p binding energy suggests that Co replaces the tetrahedral Zn sites, consistent with the XRD analysis results.[35,39] The increase in In 3d binding energy may result from the combined effects of structural deformation, synergistic effects, and electron compensation mechanisms, consistent with the literature reporting a decrease in all energies.[40] For Co, the binding energies of Co $2p_{1/2}$ and $2p_{3/2}$ are 794.8 eV and 779.9 eV (SI S5), respectively, consistent with the characteristic peaks of Co^{2+}.[41] This indicates that Co is incorporated into the ZIS lattice as Co^{2+}, consistent with the XRD analysis results.

The crystalline structure of the synthesized materials was characterized by X-ray diffraction (XRD), as shown in Fig. 2e.

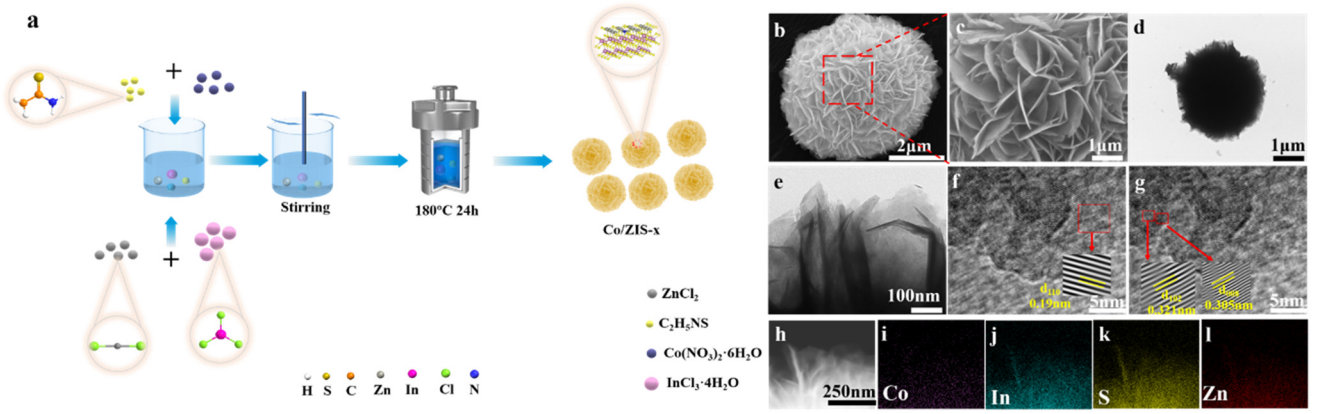

Fig. 1 (a)The synthesis schematic diagram of Co/ZIS-*x*; (b and c) SEM images of Co/ZIS-2; (d and e) TEM images of Co/ZIS-2; (f and g) HRTEM images of Co/ZIS-2; (h–l) EDS characterization of Co/ZIS-2.

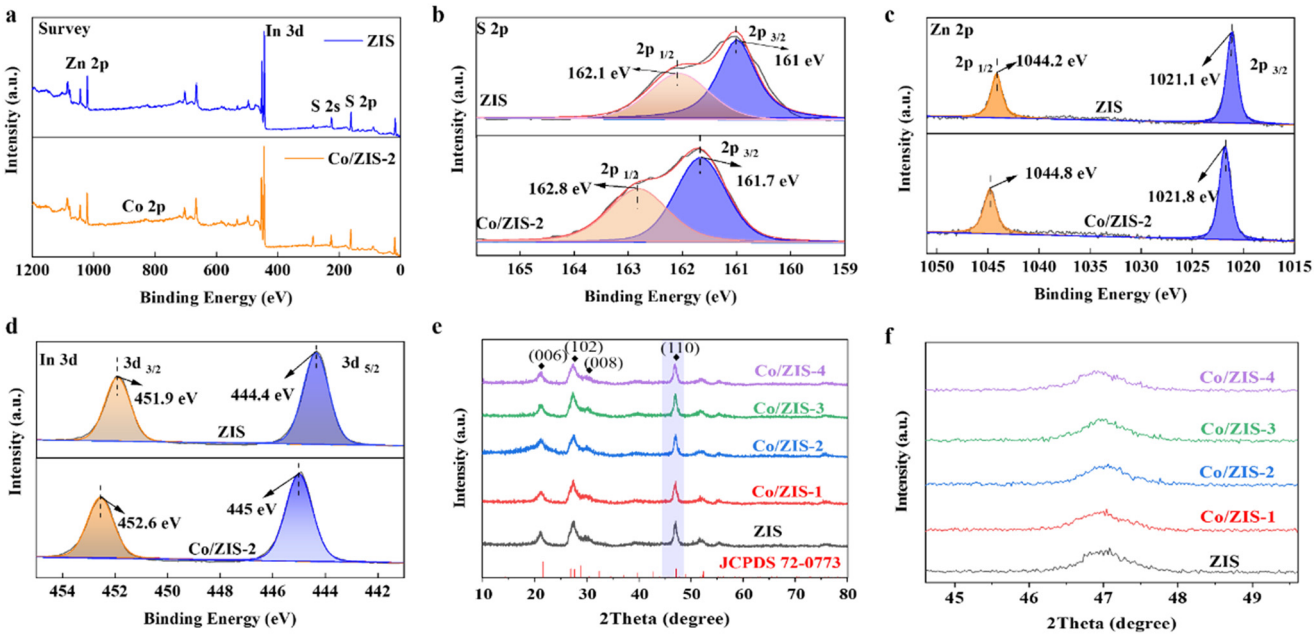

Fig. 2 (a) XPS survey spectra of ZIS and Co/ZIS-2; (b–d) XPS spectra of S 2p, Zn 2p, and In 3d. (e) XRD patterns of ZIS and Co/ZIS-*x*; (f) XRD patterns of the (110) plane for Co/ZIS-*x*.

The characteristic peaks of all samples correspond to the hexagonal phase of $ZnIn_2S_4$ (JCPDS 72-0773), exhibiting strong peaks of $ZnIn_2S_4$.[35] No peaks corresponding to impurities like ZnS or In_2S_3 are observed in the XRD patterns, highlighting the purity of the prepared samples. The XRD patterns of the prepared samples are similar, indicating that Co^{2+} doping during the hydrothermal process does not affect the crystalline structure of $ZnIn_2S_4$. This is because the ionic radii of Co^{2+} and Zn^{2+} are nearly identical (0.072 Å and 0.074 Å), respectively.[42,43] Therefore, when Co^{2+} substitutes for Zn^{2+}, the impact on lattice parameters is negligible. All the synthesized samples show nearly identical peaks. Additionally, Cu^{2+}, with an ionic radius identical to Co^{2+}, easily substitutes Zn^{2+} during the hydrothermal process.[44] As the doping concentration increases, the diffraction peak corresponding to the (110) plane shifts slightly towards higher angles, indicating that doping reduces the crystal's interplanar spacing (Fig. 2f). Combining the XRD, HRTEM, and XPS results, it can be concluded that a series of Co-doped ZIS materials have been successfully synthesized.

3.2 Photocatalytic HMF oxidation

First, we synthesized a series of metal sulfides: $CdIn_2S_4$, $CuIn_2S_4$, CuS, and $ZnIn_2S_4$. Under irradiation with 450 nm monochromatic light, only $CdIn_2S_4$ and $ZnIn_2S_4$ showed photocatalytic activity in acetonitrile (SI Fig. S6). The photocatalytic activity of $CdIn_2S_4$ is lower than that of $ZnIn_2S_4$,

and Cd is a harmful heavy metal to human health. Therefore, we focused our study on $ZnIn_2S_4$. We further investigated the photocatalytic activity of the prepared samples. Fig. 3a illustrates the photocatalytic activity of $ZnIn_2S_4$ with varying Co doping levels under a simple hydrothermal process and exposure to 450 nm monochromatic light. As shown in Fig. 3a, under 450 nm light, the pristine material exhibits photocatalytic activity with a conversion rate of 70% and a yield of 53%, but its selectivity is only 75%, suggesting relatively poor performance. This is due to rapid electron–hole recombination and low carrier utilization in unmodified $ZnIn_2S_4$. Upon doping with varying amounts of Co, HMF activity was significantly enhanced. The best catalyst Co/ZIS-2 achieved an 82% yield of DFF with a selectivity of 87%. The optimal catalyst bar in Fig. 3a (Co/ZIS-2) is the average of two independent runs (acetonitrile, no scavenger), $n = 2$. Thus, the single-run values in Fig. 3c and d differ slightly from the averaged bar in Fig. 3a. The yield of DFF is 410 μmol g^{-1} h^{-1}, which outperforms the photocatalytic effects reported in previous studies (SI Fig. S7). This indicates that Co strengthens the photocatalytic activity of $ZnIn_2S_4$. We investigated the time-dependent variation curve of HMF photocatalyzed by Co/ZIS-2, shown in Fig. 3b. HMF underwent rapid conversion in the first hour, and the yield of DFF reached its optimum at 5 hours, with a yield of 80%. As time progresses, the yield of DFF gradually decreases, possibly due to over-oxidation of DFF to by-products like FFCA (SI Fig. S8). Therefore, the optimal reaction time was selected to be 5 hours. The activity of Co/ZIS-2 under different reaction atmospheres is presented in Fig. 3c. In the absence of light, HMF did not undergo conversion, indicating that visible light is essential for the transformation of HMF to DFF. We investigated the conversion activity of Co/ZIS-2 under nitrogen conditions. The experimental results showed that under a nitrogen atmosphere, the yield of DFF was only 4.3%. Under an inert gas atmosphere, Co/ZIS-2 showed poor photocatalytic activity. Interestingly, under air and oxygen conditions, both the conversion rate of HMF and the yield of DFF increased significantly, indicating that oxygen plays a crucial role in the catalytic process. Under an air atmosphere, the catalytic activity of Co/ZIS-2 towards HMF is slightly lower than under an oxygen atmosphere. This may be due to the lower oxygen concentration in air compared to pure oxygen, resulting in insufficient ROS during the catalytic process and slightly reduced catalytic activity. Since ROS are required in this photocatalytic system, different quenchers were added during the reaction to investigate the active species involved, as shown in Fig. 3d. The addition of TEOA as a hole scavenger significantly suppressed HMF conversion, indicating that the photocatalytic transformation of HMF to DFF involves holes. Upon adding DMPO, no corresponding products were observed, and the conversion rate of HMF was significantly reduced, indicating that the transformation of HMF to DFF is mediated by radicals. Furthermore, adding BQ as a superoxide radical scavenger markedly suppressed the yield of DFF, further confirming the catalytic role of superoxide radicals as active species. FA was also added as a scavenger for singlet oxygen, and the yield of DFF was further suppressed. The trapping experiments indicate that the active species in the photocatalytic process include h^+, $\cdot O_2^-$, and $^1O_2$. Additionally, we investigated the effect of the reaction solvent on the photocatalytic aerobic oxidation of HMF (Fig. 3e). In water,

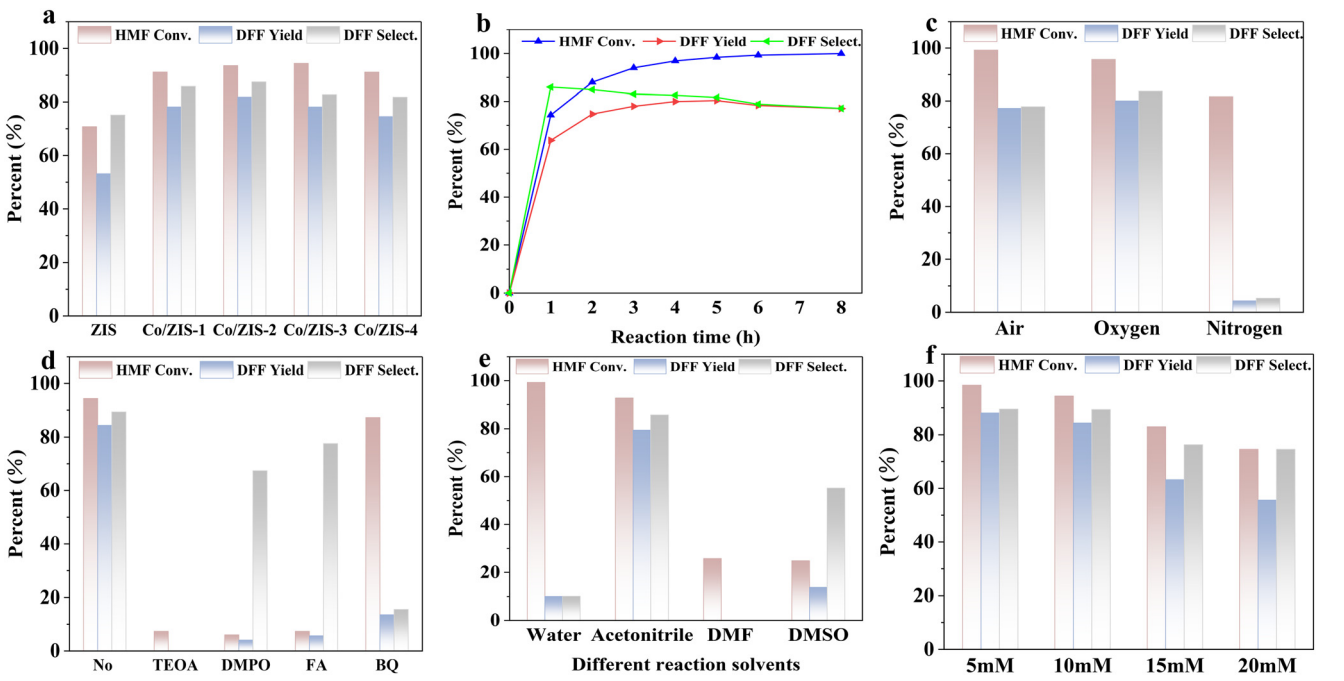

Fig. 3 (a) Activity plot for photocatalytic HMF oxidation; (b) plot of Co/ZIS-2 reactivity over time; (c) activity plot under different reaction atmospheres; (d) activity plot with various scavengers; (e) activity plot in different reaction solvents; (f) activity plot at different reaction concentrations. Standard reaction conditions: 10 mM HMF, 20 mg catalyst loading, reaction temperature: 20 °C.

HMF shows a high conversion rate but a very low yield. This is due to the generation of hydroxyl radicals (·OH) in water, which attack HMF molecules and lead to their mineralization into H_2O and CO_2. In DMF, no DFF was formed, and in DMSO, Co/ZIS-2 exhibited only weak photocatalytic activity. Clearly, acetonitrile is the optimal solvent for the photocatalytic aerobic oxidation of HMF, due to its suitable polarity, good oxygen solubility, and minimal ·OH generation. Fig. 3f illustrates the photocatalytic activity at different HMF concentrations. The yield of DFF decreases as the reactant concentration increases. This is because at low concentrations, ROS are efficiently utilized, leading to the enhanced conversion of HMF and yield of DFF. Conversely, at higher HMF concentrations, ROS are insufficient for the transformation of HMF to DFF, reducing reaction effectiveness and the yield of DFF.[45] At the optimal substrate concentration (5 mM), the yield of DFF can reach 88%, with selectivity close to 90%.

The optical absorption edges of the prepared samples were characterized using UV-vis DRS (Fig. 4a). Pure ZIS exhibited a maximum absorption wavelength of 506 nm, which shifted to 560 nm upon Co doping. Compared to the undoped ZIS, the absorption edge of Co/ZIS-2 exhibits a redshift. Co/ZIS-2 exhibits superior light absorption properties in the visible region, with characteristic peaks located within the range of 600 to 800 nm, which are attributed to the spin-state transitions from the $^2E(G)$, $^4T_1(P)$, and $^2A_1(G)$ to $^4A_2(F)$ of Co^{2+} with spin states. This result further confirms the effective incorporation of Co, implying that under visible light irradiation, electrons in the filled e energy level can be excited to the unoccupied t_2 energy level.[46,47] The Tauc plots shown in Fig. 4b were used to determine the band gaps for both ZIS and Co/ZIS-2. The optical band gap (E_g) was calculated by extrapolating the linear portion of the curve within the band edge region to the ($\alpha h\nu$) axis intercept, where $(h\nu)^{1/2} = 0$. The calculation formula is: $(\alpha h\nu)^{1/2} = A(h\nu - E_g)$.[48] After calculation, the band gap energies (E_g) of ZIS and Co/ZIS-2 are 2.69 eV and 2.47 eV, respectively. This indicates that metal ion doping narrows the band gap of ZIS, enhancing its visible light absorption and potentially improving photocatalytic activity. The valence and conduction band structures were further investigated using XPS valence band measurements (SI S9). According to XPS valence band measurements, the valence band positions for ZIS and Co/ZIS-2 are found to be 1.49 eV and 1.4 eV, respectively. The conduction band positions were calculated using the equation E_g = VB − CB, yielding values of −1.2 eV and −1.07 eV, respectively. The band positions are detailed in SI S9, and the results indicate that both materials can generate $\cdot O_2^-$ under visible light.

Photoelectrochemical measurements were conducted on the prepared samples to investigate the separation and transfer efficiencies of photogenerated charge carriers. As shown in Fig. 4c, Co/ZIS-2 exhibits a higher transient photocurrent density than ZIS, indicating improved separation efficiency of photogenerated e^- and h^+. Electrochemical impedance spectroscopy (EIS) was used to investigate charge transfer

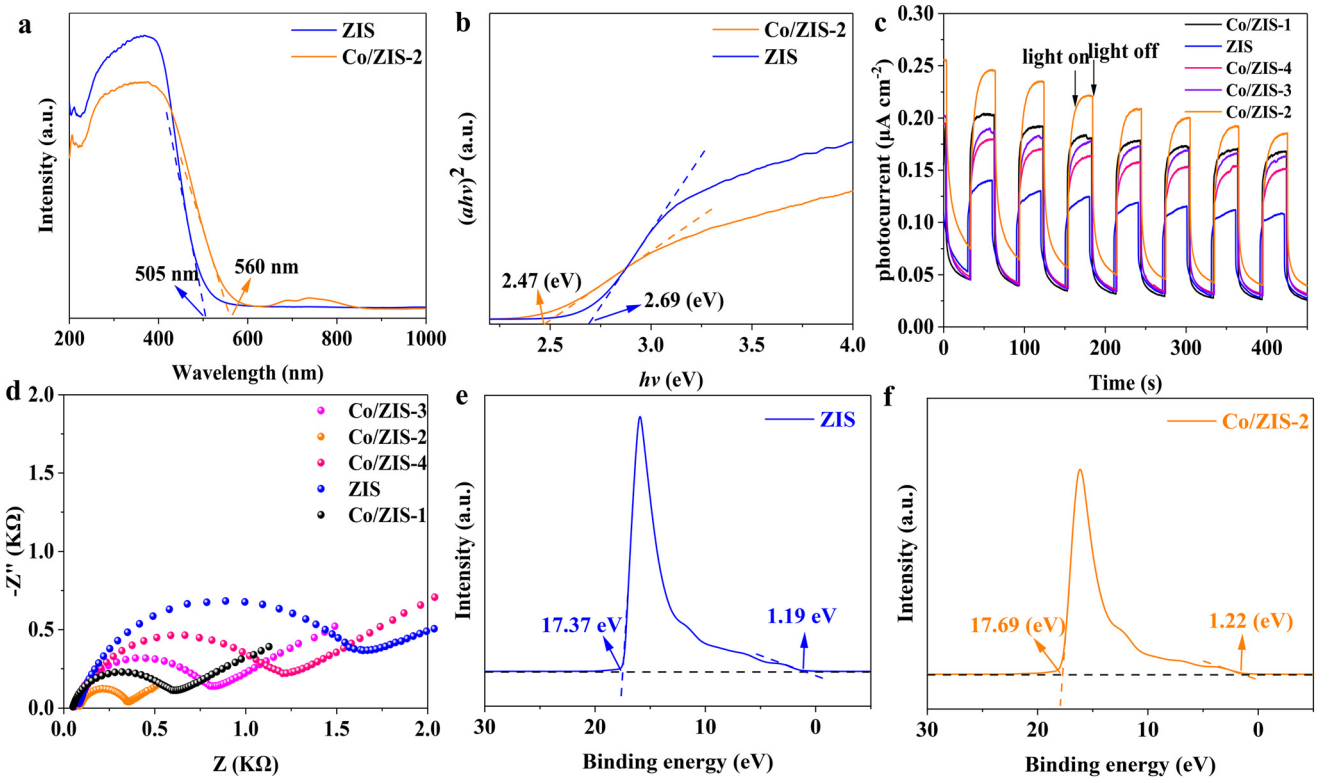

Fig. 4 (a and b) UV-vis and band gap plots of ZIS and Co/ZIS-2. (c) Transient photocurrent density and (d) Nyquist plots of Co/ZIS-*x* (*x* = 1, 2, 3, and 4). (e and f) XPS VB spectra of ZIS and Co/ZIS-2. (e) ZIS. (f) Co/ZIS-2.

resistance. In the Nyquist plot, Co/ZIS-2 exhibits a significantly smaller arc than bare ZIS (Fig. 4d), indicating lower charge transfer resistance for Co/ZIS-2 than for ZIS. This leads to higher separation and transport efficiencies of photogenerated charge carriers compared to pure ZIS, enhancing the photocatalytic activity of doped ZIS.[49] The work function, crucial for elucidating interfacial charge transfer mechanisms, was further investigated in ZIS after Co doping using UPS (Fig. 4e and f). The cutoff and Fermi edge energies of ZIS are 17.37 eV and 1.19 eV, respectively, while those of Co/ZIS-2 are 17.69 eV and 1.22 eV, respectively. Using the work function calculation formula $\Phi = 21.22 - \Delta E$ ($\Delta E = E_{cutoff} - E_{Fermi}$) and the He I UPS excitation energy of V eV, the work functions of ZIS and Co/ZIS-2 were determined to be 5.04 eV and 4.75 eV, respectively.[50] The calculated results indicate that Co/ZIS-2 possesses a smaller work function, which suggests that electron escape from ZIS becomes more facile after Co^{2+} doping. This facilitates the accumulation of electrons on the ZIS surface, which is conducive to the generation of more ROS.[51,52] The efficiency of photo-induced carrier separation was investigated using photoluminescence spectroscopy (results in SI S10). The lower the PL intensity of the photocatalytic material, the greater the degree of suppression of carrier recombination and the higher the photocatalytic activity.[53] These samples exhibit light absorption in the visible range. However, Co/ZIS-2 has lower PL intensity than pure ZIS, indicating that doping enhances electron–hole pair separation efficiency in ZIS. This accelerates the separation rate of photogenerated electron–hole pairs and the migration of photogenerated carriers, thereby significantly improving photocatalytic activity.

To elucidate the impact of doping on ZIS more comprehensively, density functional theory (DFT) calculations were performed on both pristine and doped ZIS. The calculated results, as depicted in Fig. 5, include the band structure (Fig. 5a and b) and work function of ZIS (Fig. 5c and d) before and after the doping process. The results show that Co doping decreases the band gap from 0.68 eV to 0.53 eV, and this trend is consistent with UV data, indicating that Co doping reduces the energy required for electrons to transition from the valence band to the conduction band by altering the electronic state distribution. The work function of pristine ZIS (6.056 eV) was found to be significantly higher than that of Co/ZIS-2 (5.42 eV), which is consistent with the experimental results obtained from UPS measurements. DFT calculations further substantiate that the incorporation of Co dopants into ZIS significantly enhances its catalytic activity.

3.3 Photocatalytic mechanism

To gain deeper insights into the impact of Co site introduction on ZIS, the *in situ* XPS technique was employed to analyze the binding energy variations of S, In and Zn elements before and after light irradiation. As illustrated in Fig. 6a–f, the *in situ* XPS analysis reveals that under light irradiation, the binding energies of S and Zn elements exhibit negative shifts, while those of the In element remain essentially unchanged. Following the introduction of Co sites, the S, In and Zn elements exhibit more pronounced negative shifts in binding energy compared to the pristine ZIS. This observation suggests

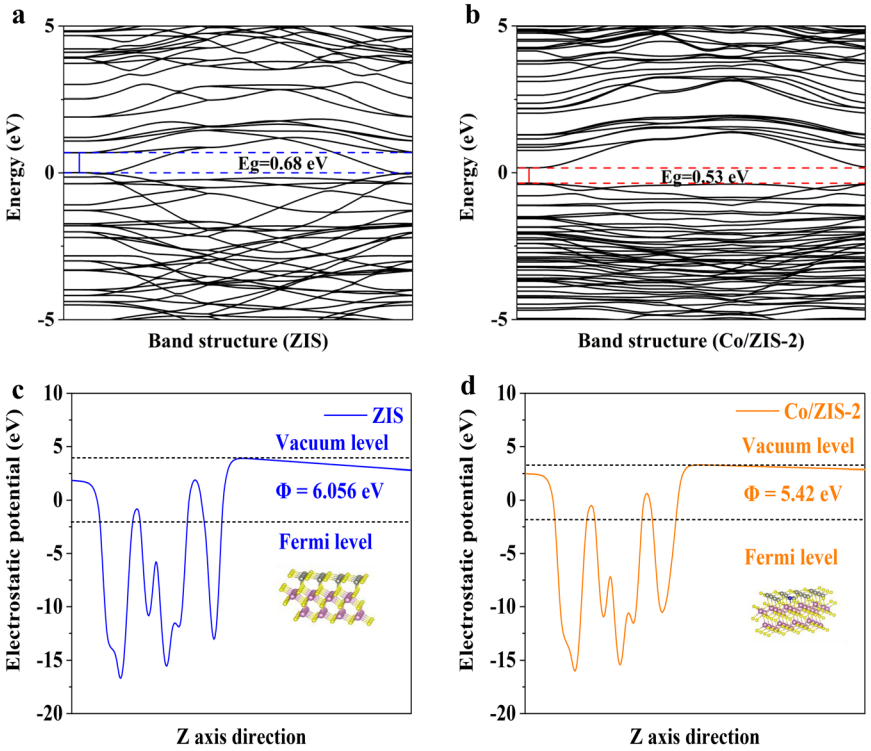

Fig. 5 (a and b) DFT calculated band structure. (a) ZIS (b) Co/ZIS-2. (c and d) Electrostatic potential and work function of ZIS and Co/ZIS-2. (c) ZIS (d) Co/ZIS-2.

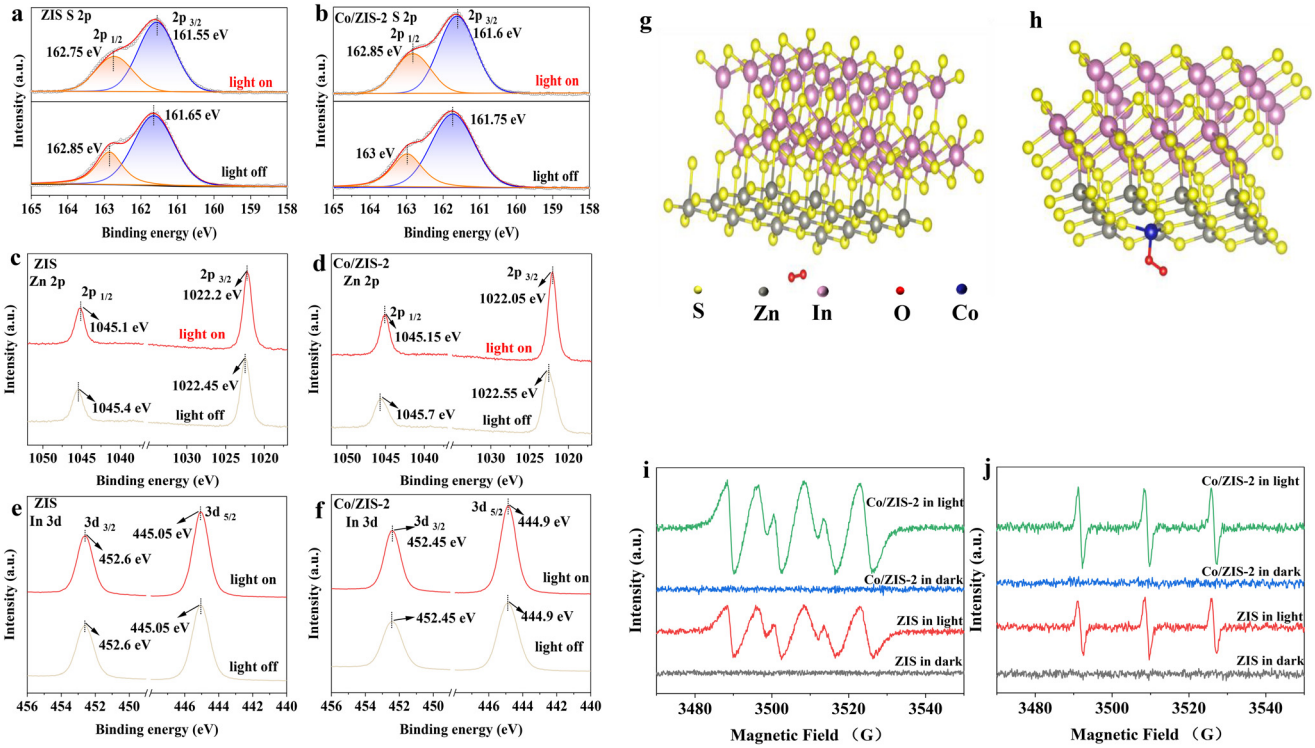

Fig. 6 XPS spectra of ZIS and Co/ZIS-2 in the dark and under light irradiation: (a and b) S 2p, (c and d) Zn 2p, and (e and f) In 3d. (g) The oxygen adsorption model of ZIS. (h) The oxygen adsorption model of Co/ZIS-2. (i) Comparative EPR signals of $\cdot O_2^-$ for Co/ZIS-2 and ZIS. (j) Comparative EPR signals of $^1O_2$ for Co/ZIS-2 and ZIS.

that photogenerated electrons are transferred and accumulated around these elements under light irradiation, subsequently participating in photocatalytic reactions. *In situ* Fourier-transform infrared spectroscopy (FTIR) was employed to probe the oxygen adsorption dynamics on both pristine ZIS and Co/ZIS-2 surfaces, as shown in SI Fig. S11. Interestingly, infrared spectroscopy analysis revealed that neither ZIS nor Co/ZIS-2 exhibited corresponding oxygen adsorption peaks over time. Oxygen adsorption spectroscopy revealed comparable adsorption capacities between ZIS and Co/ZIS-2, suggesting that cobalt incorporation exerts a negligible effect on enhancing the chemisorption of molecular oxygen under ambient reaction conditions. Complementary DFT calculations were systematically conducted to probe the oxygen adsorption energetics evolution upon cobalt doping, as detailed in SI Fig. S11 and 6g and h. The DFT computations revealed nearly identical adsorption free energies of −0.02 eV for pristine ZIS and −0.03 eV for Co/ZIS-2, exhibiting no substantial disparity (ΔG < 0.01 eV). This computational evidence conclusively demonstrates the negligible enhancement in oxygen adsorption capacity induced by cobalt modification under operational conditions, in remarkable agreement with *in situ* FTIR spectroscopic observations. Fig. 6i presents the EPR results of $\cdot O_2^-$, exhibiting a characteristic four-peak pattern, which confirms the presence of $\cdot O_2^-$. At 0 minutes in the dark, the spectrum displays minimal intensity, whereas under light irradiation, its peak intensity is significantly higher than that of ZIS. Under illumination, Fig. 6j shows the EPR results of $^1O_2$, revealing a characteristic three-peak pattern, which confirms the presence of $^1O_2$. The peak intensity of Co/ZIS-2 is significantly higher than that of ZIS. The EPR results show that the predominant ROS generated during the catalytic process are $\cdot O_2^-$ and $^1O_2$. The *in situ* FTIR spectroscopy results demonstrated that the oxygen adsorption capacity of ZIS was not further enhanced after doping. However, the EPR analysis revealed that Co^{2+}-doped ZIS generated significantly more ROS. This phenomenon can be attributed to the reduced carrier recombination rate and improved utilization efficiency of photogenerated charge carriers in the doped ZIS under visible-light irradiation, which aligns with the findings from photoelectrochemical characterization. Consequently, the enhanced ROS generation in doped ZIS effectively boosted the photocatalytic activity toward HMF oxidation.

Fig. 7a and b, and S12 illustrate the simulated density of states (DOS) for both the unmodified ZIS and Co/ZIS-2 catalysts. The incorporation of Co^{2+} into the pristine ZIS alters the composition and contribution of the conduction band minimum (CBM), indicating the electron-rich nature of Co^{2+}. The adsorption energies of HMF and DFF molecules were calculated and analyzed using DFT, both before and after doping (Fig. 7c–g). The computational results show that the adsorption energy of HMF molecules and the desorption energy of DFF molecules on catalyst ZIS are −1.20 eV and 0.51 eV, respectively, while on catalyst Co/ZIS-2, these values are −0.67 eV and −0.35 eV, respectively. The computational results suggest that DFF molecule desorption from Co/ZIS-2

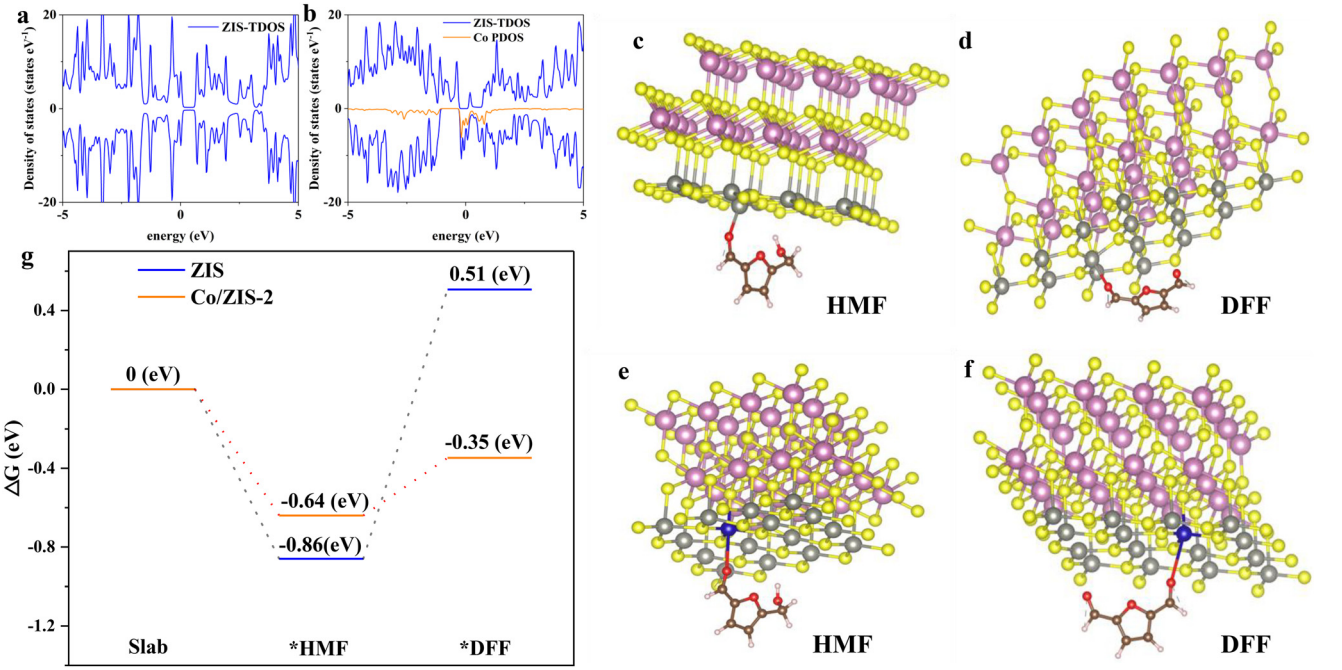

Fig. 7 DFT calculations and the proposed schematic reaction process. (a and b) TDOS of ZIS and Co/ZIS-2 and Co PDOS of Co/ZIS-2. (c and d) Adsorption of HMF molecules by ZIS and desorption of DFF. (e and f) Adsorption of HMF molecules by Co/ZIS-2 and desorption of DFF. (g) DFT calculations of adsorption/desorption free energy diagrams for HMF and DFF on ZIS and Co-doped ZIS-2.

is thermodynamically spontaneous, while desorption from ZIS requires a higher energy barrier. Prompt desorption of DFF molecules facilitates the utilization of active sites, thereby enhancing photocatalytic activity. Combining DFT calculations with ESR evidence for enhanced $\cdot O_2^-$ and $^1O_2$ formation, we find that Co sites exert a dual role: they modestly amplify active oxygen species and, more critically, lower the DFF desorption energy from +0.51 eV to −0.35 eV. This thermodynamic shift enables spontaneous and rapid DFF release, preventing over-oxidation and sustaining efficient HMF → DFF turnover.[57]

The recyclability of the catalyst was also investigated. After the reaction, the solution was washed alternately with ethanol and acetonitrile, and then dried overnight for reuse. The catalytic activity significantly decreased after three reaction cycles (SI S13). To identify the cause of the photocatalytic activity decline, the recovered catalyst was subjected to XRD analysis (SI S13). After the cyclic reactions, the crystallinity of Co/ZIS-2

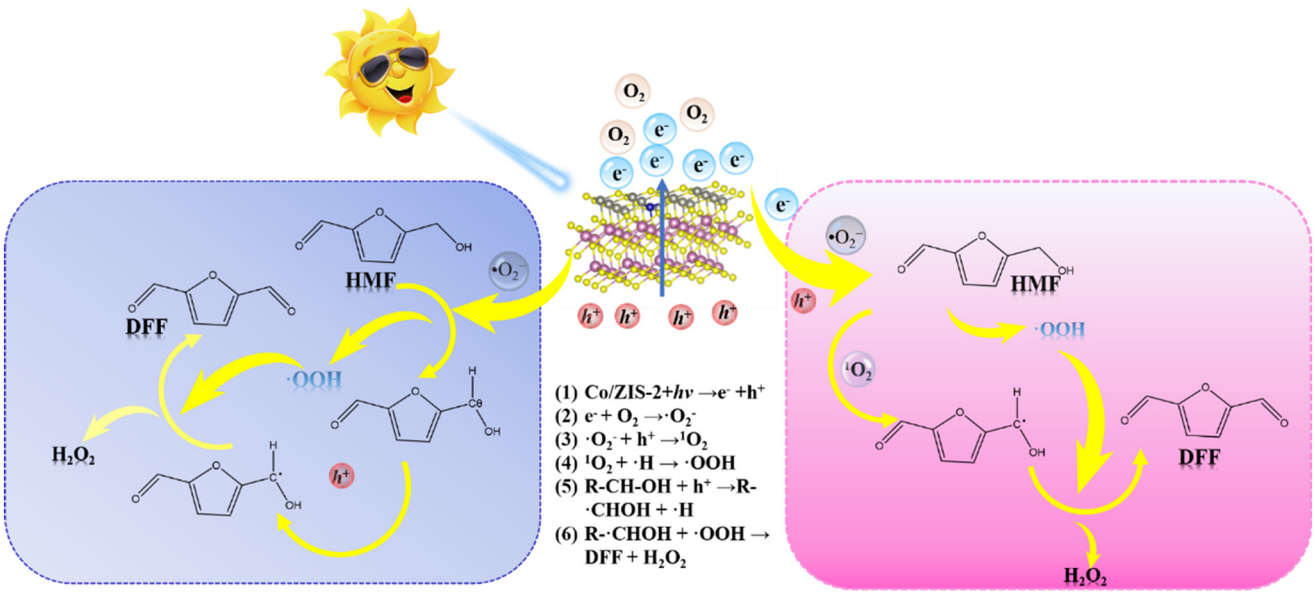

Fig. 8 Schematic diagram of the photocatalytic mechanism.

decreased significantly compared to the fresh catalyst, and the (008) crystal plane disappeared. SEM images (SI S13) show that the catalyst morphology after the reaction is no longer fluffy nanospheres, but instead covered by a layer. This coverage masks the active sites, reducing catalytic performance. Moreover, metal sulfides are prone to photocorrosion under aerobic conditions, which further degrades catalytic performance.[53] After adding a fresh catalyst, the DFF yield was restored to 63%, with a selectivity of 81%.

In addition, a trace amount of hydrogen peroxide was detected in the post-reaction solution (SI S14). Utilizing ESR analysis alongside experiments for trapping active species, we suggest a mechanism for the photocatalytic selective oxidation of HMF to DFF as follows:[25,31] under visible light, photogenerated electrons migrate to Co sites, facilitating adsorption and activation of molecular O_2. Reactive oxygen species (ROS) are formed as $\cdot O_2^-$ *via* direct reduction of O_2 or as $^1O_2$ *via* further oxidation of $\cdot O_2^-$ through photogenerated holes. Consequently, HMF molecules are selectively oxidized to DFF through two pathways: involving $\cdot O_2^-$ and $^1O_2$. In the pathway dominated by $\cdot O_2^-$, HMF molecules are attacked by $\cdot O_2^-$, forming alkoxide anions and ·OOH intermediates, which are subsequently transformed into alkoxide anion radicals by photogenerated holes. In the pathway primarily involving $^1O_2$, $^1O_2$ directly oxidizes HMF molecules to produce alkoxide anion radicals. Ultimately, these radicals and ·OOH intermediates lead to the formation of DFF molecules and H_2O_2.The aforementioned mechanism can be described by the reaction equations in Fig. 8.

4. Conclusion

In summary, we synthesized transition metal Co^{2+}-doped $ZnIn_2S_4$ microspheres for the aerobic photocatalytic conversion of HMF to the value-added chemical DFF. The Co/ZIS-2 nanoflower spheres, with an appropriate bandgap, demonstrated efficient separation of electrons (e^-) and holes (h^+) under visible light irradiation, achieving a 98% conversion rate of HMF and an 88% yield of DFF (HMF, 5 mM). Quenching experiments and electron EPR characterization were conducted to investigate the reaction mechanism, elucidating the roles of reactive species ($\cdot O_2^-$ and $^1O_2$) as well as photogenerated e^- and h^+ in the selective oxidation process. Doping modification not only enhanced the concentration of reactive species but, more importantly, facilitated surface reactions by introducing doping sites, which accelerated the desorption rate of DFF molecules and ensured the efficient utilization of catalytically active sites. This work emphasizes the role of transition metal doping in enhancing the photocatalytic activity of $ZnIn_2S_4$, offering insights into developing efficient photocatalysts for producing higher value-added chemicals from biomass.

Conflicts of interest

There are no conflicts to declare.

Data availability

The data supporting this article have been included as part of the supplementary information (SI). Supplementary information is available. See DOI: https://doi.org/10.1039/d5cy01322d.

Acknowledgements

We gratefully thank the National Natural Science Foundation of China (No. 22208127), the Senior Talent Research Foundation of Jiangsu University (No. 23JDG030, 22JDG017), the RGC Postdoctoral Fellowship Scheme of Hong Kong (RGC-PDFS-2324-2S04) and the Postgraduate Research & Practice Innovation Program of Jiangsu Province (SJCX24_2419, KYCX24_3952). This work was financially supported by the research project of Jiangsu University (Y23A145, 23A097).

References

1 P. Gallezot, Conversion of biomass to selected chemical products, *Chem. Soc. Rev.*, 2012, **41**, 1538–1558, DOI: 10.1039/C1CS15147a.
2 M. Li, H. Jiang, L. Zhang, X. Zhang, A. E.-G. A. Yagoub and C. Zhou, Synthesis of 5-HMF from Ultrasound-Ionic Liquid Pretreated Sugarcane Bagasse by Using Microwave-Solid Acid/Ionic Liquid System, *Ind. Crops Prod.*, 2020, **149**, 112361, DOI: 10.1016/j.indcrop.2020.112361.
3 Z. Zhu, X. Xing, Q. Qi, W. Shen, X. Yu, X. Song, H. Li, X. Zhang, J. Zhao, Y. Liang and P. Huo, Regulation CN reduction of CO_2 products selectivity by adjusting the number of V sites and mechanism exploration, *Fuel*, 2025, **388**, 134509, DOI: 10.1016/j.fuel.2025.134509.
4 C. Gong, X. Meng, C. Jin, M. Yang, K. Sheng, Y. Pu, G. Ji and X. Zhang, Green Synthesis of Cellulose Formate and Its Efficient Conversion into 5-Hydroxymethylfurfural, *Ind. Crops Prod.*, 2023, **192**, 115985, DOI: 10.1016/j.indcrop.2022.115985.
5 L. Hu, L. Lin, Z. Wu, S. Zhou and S. Liu, Recent Advances in Catalytic Transformation of Biomass-Derived 5-Hydroxymethylfurfural into Innovative Fuels and Chemicals, *Renewable Sustainable Energy Rev.*, 2017, **74**, 230–257, DOI: 10.1016/j.rser.2017.02.042.
6 Q. Gao, Y. Wang, Y. Li, J. Hou, Y. Liang and Z. Zhang, Investigation of the Formation of Furfural Compounds in Apple Products Treated with Pasteurization and High Pressure Processing, *Food Res. Int.*, 2024, **190**, 114546, DOI: 10.1016/j.foodres.2024.114546.
7 A. Serrano, E. Calviño, J. Carro, M. I. Sánchez-Ruiz, F. J. Cañada and A. T. Martínez, Complete Oxidation of Hydroxymethylfurfural to Furandicarboxylic Acid by Aryl-Alcohol Oxidase, *Biotechnol. Biofuels*, 2019, **12**, 217, DOI: 10.1186/s13068-019-1555-z.
8 C. Li, J. Li, L. Qin, P. Yang and D. G. Vlachos, Recent Advances in the Photocatalytic Conversion of Biomass-Derived Furanic Compounds, *ACS Catal.*, 2021, **11**, 11336–11359, DOI: 10.1021/acscatal.1c02551.
9 C. A. Antonyraj, B. Kim, Y. Kim, S. Shin, K.-Y. Lee, I. Kim and J. K. Cho, Heterogeneous Selective Oxidation of

5-Hydroxymethyl-2-furfural (HMF) into 2,5-Diformylfuran Catalyzed by Vanadium Supported Activated Carbon in MIBK, Extracting Solvent for HMF, *Catal. Commun.*, 2014, **57**, 64–68, DOI: 10.1016/j.catcom.2014.08.008.

10 K. Ghosh, R. A. Mollaa, M. A. Iqubal, S. M. Islam and S. M. Islam, Ruthenium Nanoparticles Supported on N-Containing Mesoporous Polymer Catalyzed Aerobic Oxidation of Biomass-Derived 5-Hydroxymethylfurfural (HMF) to 2,5-Diformylfuran (DFF), *Appl. Catal., A*, 2016, **520**, 44–52, DOI: 10.1016/j.apcata.2016.03.035.

11 H. Jian, K. Deng, T. Wang, C. Huang, F. Wu, H. Huo, B. Ouyang, X. Liu, J. Ma, E. Kan and A. Li, High-Density Triple-Phase Contact Points for Enhanced Photocatalytic CO_2 Reduction to Methanol, *Chin. Chem. Lett.*, 2024, **35**, 108651, DOI: 10.1016/j.cclet.2023.108651.

12 Y. Xu, M. M. Hassan, S. Ali, H. Li, Q. Ouyang and Q. Chen, Self-Cleaning-Mediated SERS Chip Coupled Chemometric Algorithms for Detection and Photocatalytic Degradation of Pesticides in Food, *J. Agric. Food Chem.*, 2021, **69**(6), 1667–1674, DOI: 10.1021/acs.jafc.0c06513.

13 J. Li, Z. Zhao, Z. Li, H. Yang, S. Yue, Y. Tang and Q. Wang, Construction of Immobilized Films Photocatalysts with CdS Clusters Decorated by Metal Cd and BiOCl for Photocatalytic Degradation of Tetracycline Antibiotics, *Chin. Chem. Lett.*, 2022, **33**, 3705–3708, DOI: 10.1016/j.cclet.2021.10.080.

14 Q. Qi, Z. Liu, Y. Li, Y. Fang, X. Tang, Z. Zhu, Y. Yan and P. Hu, Switching Photocatalytic CO_2 Reduction Path via Controlled Surface Hydroxylation in GO/CoTPP Hybrids, *Inorg. Chem.*, 2025, **64**, 19085–19093, DOI: 10.1021/acs.inorgchem.5c03491.

15 Q. Qi, W. Shen, Y. Yan, Y. Fang, Y. Zhang, X. Tang and P. Hu, Construction of In-modified CN-based photocatalyst with In–N chemical bond for efficient photoreduction of CO_2, *J. Mater. Sci. Technol.*, 2026, **261**, 161–170, DOI: 10.1016/j.jmst.2025.08.061.

16 Y. Wan, H. Wang, J. Liu, Y. Lei, W. Ma, X. Song, W. Zhou, X. Liu, J. Zhang, B. Li and P. Huo, Fabricated S-Scheme CoS/CeO_2 Heterojunction Photocatalyst Efficiently Activates Peroxymonosulfate for Polyethylene Terephthalate Plastic Degradation: Insight into Radicals and Electron Transfer, *Chem. Eng. J.*, 2024, **502**, 158124, DOI: 10.1016/j.cej.2024.158124.

17 L. Jiang, W. Wei, S. Liu, S. A. Haruna, M. Zareef, W. Ahmad, M. M. Hassan, H. Li and Q. Chen, A Tailorable and Recyclable TiO_2 NFSF/Ti@Ag NPs SERS Substrate Fabricated by a Facile Method and Its Applications in Prohibited Fish Drugs Detection, *J. Food Meas. Charact.*, 2022, **16**, 2890–2898, DOI: 10.1007/s11694-022-01401-6.

18 X. Bao, M. Liu, Z. Wang, D. Dai, P. Wang, H. Cheng, Y. Liu, Z. Zheng, Y. Dai and B. Huang, Photocatalytic Selective Oxidation of HMF Coupled with H_2 Evolution on Flexible Ultrathin g-C_3N_4 Nanosheets with Enhanced N–H Interaction, *ACS Catal.*, 2022, **12**, 1919–1929, DOI: 10.1021/acscatal.1c05357.

19 J. Kim, H. Lee and H. S. Kim, MoS_2/CdS Nanocomposites for HMF Photocatalytic Conversion to DFF under Visible Light Irradiation, *ACS Appl. Nano Mater.*, 2024, **7**(23), 23205–23213, DOI: 10.1021/acsanm.4c04577.

20 T. Shan, L. Luo, T. Chen, L. Deng, M. Li, X. Yang, L. Shen and M. Q. Yang, Visible-light-driven anaerobic oxidative upgrading of biomass-derived HMF for co-production of DFF and H_2 over a 1D $Cd_{0.7}Zn_{0.3}S$/$NiSe_2$ Schottky junction, *Green Chem.*, 2023, **25**, 2745–2756, DOI: 10.1039/d3gc00026e.

21 V. R. Battula, A. Jaryal and K. Kailasam, Visible light-driven simultaneous H_2 production by water splitting coupled with selective oxidation of HMF to DFF catalyzed by porous carbon nitride, *J. Mater. Chem. A*, 2019, **7**(19), 23205–23213, DOI: 10.1039/c8ta10926e.

22 L. Wei, Y. Chen, Y. Lin, H. Wu, R. Yuan and Z. Li, MoS_2 as a non-noble-metal co-catalyst for photocatalytic hydrogen evolution over hexagonal $ZnIn_2S_4$ under visible light irradiations, *Appl. Catal., B*, 2014, **144**, 521–527, DOI: 10.1016/j.apcatb.2013.07.064.

23 C. Duan, Q. Zhang, Z. Lin, B. Yan, C. Xie and G. Yang, Half-unit-cell $ZnIn_2S_4$ monolayer with sulfur vacancies for photocatalytic hydrogen evolution, *Appl. Catal., B*, 2019, **248**, 193–201, DOI: 10.1016/j.apcatb.2019.02.027.

24 R. Yang, L. Mei, Y. Fan, Q. Zhang, R. Zhu, R. Amal, Z. Yin and Z. Zeng, $ZnIn_2S_4$-Based Photocatalysts for Energy and Environmental Applications, *Small Methods*, 2021, **5**, 2100887, DOI: 10.1002/smtd.202100887.

25 Y. Liu, W. Xue, A. Chowdhury, A. P. Rangappa and J. Zhao, S-vacancy regulation over ultra-thin $ZnIn_2S_4$ for enhanced photocatalytic valorization of biomass-derived 5-hydroxymethylfurfural to 2,5-diformylfuran, *Chem. Eng. J.*, 2024, **497**, 154613, DOI: 10.1016/j.cej.2024.154613.

26 Y. Zhu, J. Chen, L. Shao, X. Xia, Y. Li and L. Wang, Oriented facet heterojunctions on CdS nanowires with high photoactivity and photostability for water splitting, *Appl. Catal., B*, 2020, **268**, 118744, DOI: 10.1016/j.apcatb.2020.118744.

27 S. Zhang, Z. Zhang, Y. Si, B. Li, F. Deng, L. Yang, X. Liu, W. Dai and S. Luo, Gradient hydrogen migration modulated with self-adapting S vacancy in copper-doped $ZnIn_2S_4$ nanosheet for photocatalytic hydrogen evolution, *ACS Nano*, 2021, **15**, 15238–15248, DOI: 10.1021/acsnano.1c05834.

28 S. Si, P. Gong, X. Bao, X. Tan, Y. Mao, H. Zhang, D. Xiao, K. Song, Z. Wang, P. Wang, Y. Liu, Z. Zheng, Y. Dai, B. Huang and H. Cheng, Visible-Light-Driven Highly Selective 5-Hydroxymethylfurfural Upgrading and H_2 Generation via Atomically Dispersed Ni Sites on $ZnIn_2S_4$ Nanosheets, *ACS Catal.*, 2024, **14**, 8343–8352, DOI: 10.1021/acscatal.4c00123.

29 M. Gu, Y. Yang, B. Cheng, L. Zhang, P. Xiao and T. Chen, Unveiling Product Selectivity in S-Scheme Heterojunctions: Harnessing Charge Separation for Tailored Photocatalytic Oxidation, *Chin. J. Catal.*, 2024, **59**(2), 185–194, DOI: 10.1016/S1872-2067(23)64610-8.

30 Y. Zhu, W. Deng, Y. Tan, J. Shi, J. Wu, W. Lu, J. Jia, S. Wang and Y. Zou, In situ topochemical transformation of $ZnIn_2S_4$ for efficient photocatalytic oxidation of 5-hydroxymethylfurfural to 2,5-diformylfuran, *Adv. Funct. Mater.*, 2023, **33**(23), 2304985, DOI: 10.1002/adfm.202304985.

31 M. Zhang, Z. Li, X. Xin, J. Zhang, Y. Feng and H. Lv, Selective valorization of 5-hydroxymethylfurfural to 2,5-diformylfuran using atmospheric O_2 and $MAPbBr_3$ perovskite under visible light, *ACS Catal.*, 2020, **10**, 14793–14800, DOI: 10.1021/acscatal.0c04330.

32 H. Qian, Q. Hou, W. Zhang, Y. Nie, R. Lai, H. Ren, G. Yu, X. Bai, H. Wang and M. Ju, Construction of electron transport channels and oxygen adsorption sites to modulate reactive oxygen species for photocatalytic selective oxidation of 5-hydroxymethylfurfural to 2,5-diformylfuran, *Appl. Catal., B*, 2022, **319**, 121907, DOI: 10.1016/j.apcatb.2022.121907.

33 Y. Guo, B. Liu, J. Zhang, G. Wang, C. Pan, H. Zhao, C. Wang, F. Yu, Y. Dong and Y. Zhu, Perylene imide supermolecule promote oxygen to superoxide radical for ultrafast photo-oxidation of 5-hydroxymethylfurfural, *Appl. Catal., B*, 2024, **340**, 123217, DOI: 10.1016/j.apcatb.2023.123217.

34 S. Zhang, Z. Zhang, Y. Si, B. Li, F. Deng, L. Yang, X. Liu, W. Dai and S. Luo, Gradient Hydrogen Migration Modulated with Self-Adapting S Vacancy in Copper-Doped $ZnIn_2S_4$ Nanosheet for Photocatalytic Hydrogen Evolution, *ACS Nano*, 2021, **15**, 15238–15248, DOI: 10.1021/acsnano.1c05834.

35 B. Xu, B. Chong, H. Li and G. Yang, Cobalt incorporation-induced photocatalytic reactivity enhancement in $ZnIn_2S_4$ nanosheets for effective hydrogen production, *Chem. Eng. Sci.*, 2023, **280**, 118985, DOI: 10.1016/j.ces.2023.118985.

36 G. Han, X. Liu, Z. Cao and Y. Sun, Photocatalytic Pinacol C−C Coupling and Jet Fuel Precursor Production on $ZnIn_2S_4$ Nanosheets, *ACS Catal.*, 2020, **10**, 9346–9355, DOI: 10.1021/acscatal.0c01715.

37 P. Lu, K. Liu, Y. Liu, Z. Ji, X. Wang, B. Hui, Y. Zhu, D. Yang and L. Jiang, Heterostructure with tightly-bound interface between In_2O_3 hollow fiber and $ZnIn_2S_4$ nanosheet toward efficient visible light-driven hydrogen evolution, *Appl. Catal., B*, 2024, **345**, 123697, DOI: 10.1016/j.apcatb.2024.123697.

38 S. Wang, B. Yuan, B. Guan and X. W. D. Lou, Construction of $ZnIn_2S_4$–In_2O_3 hierarchical tubular heterostructures for efficient CO_2 photoreduction, *J. Am. Chem. Soc.*, 2018, **140**, 5037–5040, DOI: 10.1021/jacs.8b02200.

39 J. Xue, H. Liu, S. Zeng, Y. Feng, Y. Zhang, M. Cheng, H. Zhang, L. Shi and G. Zhang, Bifunctional cobalt-doped $ZnIn_2S_4$ hierarchical nanotubes endow noble-metal cocatalyst-free photocatalytic H_2 production coupled with benzyl alcohol oxidation, *Sol. RRL*, 2022, **6**, 2101042, DOI: 10.1002/solr.202101042.

40 S. Liu, Q. Han and X. Liu, Facile Preparation of Co-Doped $ZnIn_2S_4$ Nanosheets for Highly Efficient Photocatalytic Hydrogen Peroxide Production, *J. Alloys Compd.*, 2024, **776**, 176965, DOI: 10.1016/j.jallcom.2024.176965.

41 H. Zhong, K. H. Ly, M. Wang, Y. Krupskaya, X. Han, J. Zhang, J. Zhang, V. Kataev, B. Büchner, I. M. Weidinger, S. Kaskel, P. Liu, M. Chen, R. Dong and X. Feng, Phthalocyanine-Based Layered Two-Dimensional Conjugated Metal-Organic Framework as Highly Efficient Electrocatalyst for Oxygen Reduction Reaction, *Angew. Chem., Int. Ed.*, 2019, **58**, 10458–10464, DOI: 10.1002/anie.201907002.

42 W. Yuan, X. Liu and L. Li, Improving photocatalytic performance for hydrogen generation over Co-doped $ZnIn_2S_4$ under visible light, *Acta Phys.-Chim. Sin.*, 2013, **29**(1), 151–156, DOI: 10.3866/PKU.WHXB201210093.

43 Z. Lei, G. Ma, M. Liu, W. You, H. Yan, G. Wu, T. Takata, M. Hara, K. Domen and C. Li, Sulfur-substituted and zinc-doped $In(OH)_3$: A new class of catalyst for photocatalytic H_2 production from water under visible light illumination, *J. Catal.*, 2006, **237**, 322–329, DOI: 10.1016/j.jcat.2005.11.022.

44 S. Shionoya and Y. Tamoto, Luminescence of $ZnIn_2S_4$ and $ZnIn_2S_4$: Cu single crystals, *J. Phys. Soc. Jpn.*, 1964, **19**, 1142–1149, DOI: 10.1143/JPSJ.19.1142.

45 Y. Li, X. Wang, H. Huo, Z. Li and J. Shi, A novel binary visible-light-driven photocatalyst type-I $CdIn_2S_4$/g-C_3N_4 heterojunctions coupling with H_2O_2: Synthesis, characterization, photocatalytic activity for Reactive Blue 19 degradation and mechanism analysis, *Colloids Surf., A*, 2019, **580**, 124322, DOI: 10.1016/j.colsurfa.2019.124322.

46 Z. Chen, Y. Fang, L. Wang, X. Chen, W. Lin and X. Wang, Remarkable Oxygen Evolution by Co-Doped ZnO Nanorods under Visible Light, *Appl. Catal., B*, 2021, **296**, 120369, DOI: 10.1016/j.apcatb.2021.120369.

47 F. Lei, L. Zhang, Y. Sun, L. Liang, K. Liu, J. Xu, Q. Zhang, B. Pan, Y. Luo and Y. Xie, Atomic-Layer-Confined Doping for Atomic-Level Insights into Visible-Light Water Splitting, *Angew. Chem., Int. Ed.*, 2015, **54**, 9266–9270, DOI: 10.1002/anie.201503410.

48 C. Zhu, Q. He, W. Wang, F. Duan, F. Yang, C. Chen, C. Wang, X. Duan, S. Wang, X. Zhang, X. Duan, J. Li, H. Zhang, S. Wang, Z. Liu, Q. Chen, X. Duan, X. He, H. Zhang, W. Wang and Y. Wang, S-scheme photocatalysis induced by ZnIn2S4 nanoribbons-anchored hierarchical CeO_2 hollow spheres for boosted hydrogen evolution, *J. Colloid Interface Sci.*, 2022, **620**, 253–262, DOI: 10.1016/j.jcis.2022.04.024.

49 Y. Li, Z. Liu, Z. Li and Q. Wang, Renewable biomass-derived carbon-supported g-C3N4 doped with Ag for enhanced photocatalytic reduction of CO_2, *J. Colloid Interface Sci.*, 2022, **606**, 1311–1321, DOI: 10.1016/j.jcis.2021.08.176.

50 Y. Li, Z. Liu, Z. Li and Q. Wang, Renewable biomass-derived carbon-supported g-C_3N_4 doped with Ag for enhanced photocatalytic reduction of CO_2, *J. Colloid Interface Sci.*, 2022, **606**, 1311–1321, DOI: 10.1016/j.jcis.2021.08.176.

51 C. Du, B. Yan, Z. Lin and G. Yang, Enhanced Carrier Separation and Increased Electron Density in 2D Heavily N-Doped $ZnIn_2S_4$ for Photocatalytic Hydrogen Production, *J. Mater. Chem. A*, 2020, **8**, 207–217, DOI: 10.1039/c9ta11318e.

52 Y. Liu, Y. Sun, E. Zhao, W. Yang, J. Lin, Q. Zhong, H. Qi, A. Deng, S. Yang, H. Zhang, H. He, S. Liu, Z. Chen and S. Wang, Atomically dispersed silver-cobalt dual-metal sites synergistically promoting photocatalytic hydrogen evolution, *Adv. Funct. Mater.*, 2023, **33**, 2301840, DOI: 10.1002/adfm.202301840.

53 H. Zhao, D. Trivedi, M. Roostaeinia, X. Yong, J. Chen, P. Kumar, J. Liu, B.-L. Su, S. Larter, M. G. Kibria and J. Hu, Spatial Charge Separation on the (110)/(102) Facets of Cocatalyst-Free $ZnIn_2S_4$ for the Selective Conversion of 5-Hydroxymethylfurfural to 2,5-Diformylfuran, *Green Chem.*, 2023, **25**, 692–699, DOI: 10.1039/d2gc04362a.

54 R. Janani, G. S. Priyanga, S. Behara, A. A. Melvin, A. R. M. Shaheer, T. Thomas, B. Neppolian and S. Singh, Enhanced solar light driven hydrogen generation and environment remediation through Nd incorporated $ZnIn_2S_4$, *Renewable Energy*, 2020, **162**, 2031–2040, DOI: 10.1016/j.renene.2020.09.081.

55 L. Li, X. Huo, S. Chen, Q. Luo, W. Wang, Y. Wang and N. Wang, Solar-driven production of hydrogen peroxide and benzaldehyde in two-phase system by an interface-engineered heterostructure, *Small*, 2023, **19**, 2301865, DOI: 10.1002/smll.202301865.

56 Y. Gao, S. Qian, H. Wang, W. Yuan, Y. Fan, N. Cheng, H. Xue, T. Jiang and J. Tian, Boron-doping on the surface mediated low-valence Co centers in cobalt phosphide for improved electrocatalytic hydrogen evolution, *Appl. Catal., B*, 2023, **320**, 122014, DOI: 10.1016/j.apcatb.2022.122014.

57 H. Kotani, S. Kaida, T. Ishizuka, M. Sakaguchi, T. Ogura, Y. Shiota, K. Yoshizawa and T. Kojima, Formation and characterization of a reactive chromium(V)–oxo complex: mechanistic insight into hydrogen-atom transfer reactions, *Chem. Sci.*, 2015, **6**, 945–955, DOI: 10.1039/c4sc02285h.